INL/RPT-24-81091

Nuclear Energy Advanced Modeling and Simulation

Phase-field Modeling For Restructuring In The Dark Zone Of High Burnup UO_2

SEPTEMBER 2024

Sudipta Biswas, Larry K. Aagesen, and Pierre-Clément Simon

Idaho National Laboratory

Idaho National Laboratory

Battelle Energy Alliance manages INL for the U.S. Department of Energy's Office of Nuclear Energy

INL/RPT-24-81091

Phase-field Modeling For Restructuring In The Dark Zone Of High Burnup UO_2

Sudipta Biswas, Larry K. Aagesen, and Pierre-Clément Simon
Idaho National Laboratory

September 2024

Idaho National Laboratory
Computational Mechanics and Materials
Idaho Falls, Idaho 83415

http://www.inl.gov

Prepared for the
U.S. Department of Energy
Office of Nuclear Energy
Under DOE Idaho Operations Office
Contract DE-AC07-05ID14517

Page intentionally left blank

ABSTRACT

This report summarizes the mesoscale modeling work performed in fiscal year 2024 under the Nuclear Energy Advanced Modeling and Simulation (NEAMS) program to capture the microstructural evolution and restructuring observed in the dark zone of high burnup UO_2 nuclear fuel. This is the first attempt to realistically simulate the restructuring behavior observed in different regions of a high burnup fuel. We employ a grand-potential based phase-field model to concurrently evaluate the formation of subgrains and growth of fission bubbles within the fuel. A energy-based subgrain formation criteria is introduced to simulate the restructuring process. The effect of different initial conditions and different modeling parameters are studied systematically to capture how each of these parameters influence the characteristics of the restructured fuel. It is observed that the subgrain formation begins around existing fission gas bubbles and then proceeds towards triple junctions, grain boundaries and grain interiors. It is demonstrated that restructuring is influenced by a combination of initial dislocation densities, subgrain formation rate, and temperature. The rate of restructuring increases with increase in fuel temperature. A restructuring bias is observed within the microstructure due to variation in defect accumulation among different grains. Furthermore, bubble sizes and distribution do not have a significant effect on rate of restructuring. The predicted microstructures are consistent with experimental observations of the restructured regions. Finally, a correlation is presented that demonstrates the evolution of the restructuring volume fraction as a function of local effective burnup. This work provides a first of its kind restructuring model for the dark zone that can be used by BISON for performance prediction of high burnup UO_2 fuel.

Page intentionally left blank

ACKNOWLEDGEMENT

This report has been funded by the Nuclear Energy Advanced Modeling and Simulations (NEAMS) program within the U.S. Department of Energy Office of Nuclear Energy. This report was authored by Battelle Energy Alliance, LLC, a contractor of the U.S. Government under contract DE-AC07-05ID14517. Accordingly, the U.S. Government retains a non-exclusive, royalty-free license to publish or reproduce the published form of this report, or allow others to do so, for U.S. Government purposes. This research made use of the resources of the High Performance Computing Center at Idaho National Laboratory, which is supported by the DOE Office of Nuclear Energy and the Nuclear Science User Facilities under contract no. DE-AC07-05ID14517.

Page intentionally left blank

CONTENTS

Page intentionally left blank

FIGURES

Page intentionally left blank

TABLES

Page intentionally left blank

Page intentionally left blank

Phase-field modeling for restructuring in the dark zone of high burnup UO_2

1. INTRODUCTION

To improve the economics of commercial nuclear reactors, U.S. nuclear industries are seeking approval for the increased burnup usage of the existing nuclear fleet past the current regulatory limit of 62 MWd/kgU up to 75 MWd/kgU. However, at higher burnups, nuclear fuels undergo significant restructuring which poses the risks of potential fuel fragmentation, relocation, and dispersal (FFRD) during a loss-of-coolant accident (LOCA). Specifically, the regions exposed to high burnup and low temperatures exhibit a fine-grained microstructure with large bubbles known as a high-burnup structure (HBS) [4]. Furthermore, recent analysis of high burnup fuel revealed that restructuring occurs not only in the rim region, but also at another region closer to the fuel center [3, 5], sometimes referred to as the dark zone. Restructuring in the high burnup fuel has been correlated to the diminished performance of the fuel, leading to an accelerated fission gas release, as well as fuel fragmentation and pulverization during accident conditions. Therefore, it is necessary to understand the mechanisms leading to the restructuring in different regions of the fuel, along with its impact on the properties and performance of nuclear fuels.

Restructuring has been observed in various types of nuclear fuels, including ceramics and metals [6–8]. The key characteristics of the high burnup fuel include the (1) accumulation of dislocations, creating of large dislocation networks, (2) formation of new defect-free subgrains, (3) depletion of intra-granular fission gas concentration, and (4) development of large spherical inter-granular bubbles. There is a lack of consensus among researchers regarding the mechanisms that lead to the restructuring observed in high burnup fuel. Grain subdivision due to polygonization versus recrystallization, continuous versus discrete recrystallization occurring in tandem or conjunction, etc., have been proposed and debated. In general, it is hypothesized that defect accumulation and dislocation interaction within the grains cause the realignment of dislocations networks into grain boundaries (GBs), leading to the the formation of new subgrains, which over time transforms into new grains. Experimentally, advanced characterization techniques have been used on irradiated samples to study the grain structure in the partially and fully restructured fuel regions. In the high burnup fuels, both low-angle grain boundaries (LAGB) and high-angle grain boundaries (HAGB) were observed in different fractions at different radial locations. The dark zone shows higher fraction of LAGBs compared to the rim region. The low-angle character of boundaries between the subdivided grains disappeared in the fully developed HBS. It is hypothesized that defect accumulation and rearrangement due to the combination of fuel operating conditions play an important role in dictating the restructuring behavior. Localized burnup, temperature, and stress govern the characteristics of the restructured fuel in different regions.

This report provides the details of the phase-field modeling work that has been performed in fiscal year 2024 under NEAMS to capture the microstrutural evolution in the dark zone of high burnup fuel. This year we developed a phase-field model to realistically simulate the restructuring behavior observed in different regions of a high burnup fuel. We employ a grand-potential based phase-field model to concurrently evaluate the formation of subgrains and growth of fission bubbles within the fuel. The details about the model and parameterization for the dark zone are provided in Section 2. An energy-based subgrain formation criteria is introduced to simulate the restructuring process. In Section 3, the effect of different initial conditions and different modeling parameters are studied systematically to evaluate how each of these parameters influence the characteristics of the restructured fuel . Finally, the simulated microstructures are compared against the experimental observations and key findings are summarized.

2. MODEL FORMULATION

In previous years, a multiscale model coupling the phase-field model with cluster-dynamics simulations has been developed to simulate the HBS formation and associated bubble growth. It was demonstrated that the coupled model can realistically capture the convex bubble shapes typically observed in the HBS regions. In fiscal year 2024, we extend the phase-field model to capture the restructuring observed in the dark zone near the fuel center. The restructuring model presented in this section is formulated following the grand-potential-based multi-order parameter, multi-component phase-field model [9]. This model can concurrently capture the evolution of multiple phases, grains, and chemical species. Thus it enables capturing the grain structure and fission product evolution leading to microstrutural changes in a nuclear environment. The restructuring is modeled via new subgrain formation, employing a discrete nucleation approach.

2.1. Governing Equations

Here, the microstructure consists of two phases: the solid matrix and the bubble phases. Within the matrix, multiple grains are represented with different order parameters, $\eta_{m0}, \eta_{m1}, \ldots \eta_{mi}, \ldots \eta_{mn}$, while the bubbles are represented by a single order parameter, η_b. Additionally, local concentrations of vacancies and fission gases are represented as chemical components, the number densities of which are represented by ρ_v and ρ_g, respectively. The evolution of the order parameters are captured using the Allen-Cahn equations derived from the grand potential functional, such that:

$$\begin{aligned} \frac{\partial \eta_{mi}}{\partial t} &= -L_m \frac{\delta \Omega}{\delta \eta_{mi}} \\ \frac{\partial \eta_b}{\partial t} &= -L_b \frac{\delta \Omega}{\delta \eta_b}, \end{aligned} \tag{1}$$

where L_m and L_b are the kinetic mobilities of the order parameters, and $\frac{\delta \Omega}{\delta \eta_{mi}}$ and $\frac{\delta \Omega}{\delta \eta_b}$ are the variational derivatives of the grand potential Ω with respect to the order parameters η_{mi} and η_b, respectively. The total grand potential of the system, Ω, is derived from the local grand-potential densities as:

$$\Omega = \int_V \left(\omega_{bulk} + \omega_{grad} + \omega_{chem} + \omega_d\right) \mathrm{d}V \,, \tag{2}$$

where ω_{bulk} accounts for the bulk free energy density term, ω_{grad} adds the gradient energy contribution, ω_{chem} incorporates the appropriate grand-potential densities for each phases, and ω_d is the deformation energy due to dislocations. Each of these components are defined as follows:

$$\omega_{bulk} = \alpha \left[\left(\frac{\eta_b^4}{4} - \frac{\eta_b^2}{2} \right) + \sum_{i=1}^{n_m} \left(\frac{\eta_{mi}^4}{4} - \frac{\eta_{mi}^2}{2} \right) + \left(\gamma_{bm} \eta_b^2 \sum_i^{n_m} \eta_{mi}^2 + \sum_i^{n_m} \sum_{j \neq i}^{n_m} \frac{\gamma_{mm}}{2} \eta_{mi}^2 \eta_{mj}^2 \right) + \frac{1}{4} \right] , \tag{3}$$

$$\omega_{grad} = \frac{\kappa}{2} \left(|\eta_b|^2 + \sum_{i=1}^{n_m} |\nabla \eta_{mi}|^2 \right) , \tag{4}$$

$$\omega_{chem} = h_b \omega_b + h_m \omega_m \,, \tag{5}$$

and

$$\omega_d = \frac{1}{2} G \, b_g^2 \, d_{eff} \,. \tag{6}$$

Here, m and b represent the matrix and bubble phases, respectively, i and j are indices for the grains, n_m is the total number of grains, and α is a constant free energy barrier coefficient. γ_{mb} and γ_{mm} are constant

parameters that allow adjustment of interfacial energies between phases and grains. ω_m and ω_b represent the local grand-potential density of the matrix and bubble phases, respectively, and h_m and h_b are the switching functions used to interpolate the grand-potential densities between the phases. For the matrix and bubble phases, the switching functions are:

$$h_m = \frac{\sum_{i=1}^{n_m} \eta_{mi}^2}{\eta_b^2 + \sum_{i=1}^{n_m} \eta_{mi}^2}\,, \tag{7}$$

and

$$h_b = \frac{\eta_b^2}{\eta_b^2 + \sum_{i=1}^{n_m} \eta_{mi}^2}\,, \tag{8}$$

respectively. The additional dislocation energy density, ω_d, is added to capture the restructuring behavior. In Eq. 6, G is the shear modulus of the material, b_g is the Burgers vector, and d_{eff} is the effective dislocation density [10].

The evolution of the vacancies and gas atoms are expressed in terms of the chemical potentials μ_v and μ_g, such that:

$$\frac{\partial \mu_g}{\partial t} = \frac{1}{\chi_g}\left[\nabla \cdot (D_g \chi_g \nabla \mu_g) + s_g - \frac{\partial \rho_g}{\partial \eta_b}\frac{\partial \eta_b}{\partial t} - \sum_{i=1}^{n_m} \frac{\partial \rho_g}{\partial \eta_{mi}}\frac{\partial \eta_{mi}}{\partial t}\right] \tag{9}$$

and

$$\frac{\partial \mu_v}{\partial t} = \frac{1}{\chi_v}\left[\nabla \cdot (D_v \chi_v \nabla \mu_v) + s_v - \frac{\partial \rho_v}{\partial \eta_b}\frac{\partial \eta_b}{\partial t} - \sum_{\alpha} \sum_{i=1}^{p_\alpha} \frac{\partial \rho_v}{\partial \eta_{\alpha i}}\frac{\partial \eta_{\alpha i}}{\partial t}\right], \tag{10}$$

where D_g and D_v are the diffusion coefficients, and s_g and s_v are the source terms for the production of Xe atoms and U site vacancies, respectively. χ_g and χ_v are the susceptibilities defined as:

$$\chi_g = h_m \frac{1}{V_a^2 k_g^m} + h_b \frac{1}{V_a^2 k_g^b} \tag{11}$$

and

$$\chi_v = h_m \frac{1}{V_a^2 k_v^m} + h_b \frac{1}{V_a^2 k_v^b}, \tag{12}$$

respectively. Here, V_a is the atomic volume, k_g^b, k_v^b, k_g^m, and k_v^m are the curvatures of the parabolic free energy of the gas atoms and vacancies within the bubble and matrix phases. The grand-potential density for each phase is given by:

$$\omega_m = f_m - \mu_g \rho_g - \mu_v \rho_v\,, \tag{13}$$

and

$$\omega_b = f_b - \mu_g \rho_g - \mu_v \rho_v\,, \tag{14}$$

where f_m and f_b are the Helmholtz free energies of each phase. The parameterization of the Helmholtz free energies is described in Section 2.2.

2.2. Chemical Free Energy Density

Assuming the chemical energy of the matrix follows the ideal solution model, the Helmholtz free energy density is described as

$$\begin{aligned} f_{m,ideal} = \frac{1}{V_m}\Big\{ & RT\left[c_v \ln c_v + (1-c_v)\ln(1-c_v)\right] + N_A E_v^f c_v \\ & + RT\left[c_g \ln c_g + (1-c_g)\ln(1-c_g)\right] + N_A E_g^f c_g \Big\}, \end{aligned} \tag{15}$$

where R is the ideal gas constant, V_m is the molar volume such that $V_m = V_a N_A$, N_A is Avogadro's number, E_v^f is the formation energy of a U vacancy, E_g^f is the formation energy of a gas (Xe) atom, and T is the temperature. c_v and c_g represent the concentration of vacancies and gas atoms. To improve numerical performance, $f_{m,ideal}$ is approximated with a parabolic function

$$f_m = \frac{1}{2}k_v^m(c_v - c_v^{m,eq})^2 + \frac{1}{2}k_g^m(c_g - c_g^{m,eq})^2, \tag{16}$$

where $c_v^{m,eq}$ and $c_g^{m,eq}$ are the equilibrium concentrations of vacancies and gas atoms in the UO_2 matrix. The equilibrium concentrations are determined from the formation energies and temperature using $c_v^{m,eq} = \exp\left(-E_v^f/k_BT\right)$ and $c_g^{m,eq} = \exp\left(-E_g^f/k_BT\right)$, where k_B is the Boltzmann constant. The curvatures of the parabolas are set by assuming that when the vacancy concentration, c_v, is equal to the steady-state vacancy concentration during reactor operation, c_v^0, the chemical potential determined from the parabolic approximation is equal to the chemical potential of the ideal solution model, as described in [11]. Since $\mu = \frac{\partial f}{\partial \rho} = \frac{\partial f}{\partial c}\frac{\partial c}{\partial \rho} = V_a\frac{\partial f}{\partial c}$,

$$V_a\frac{\partial f_m}{\partial c_v}\bigg|_{c_v^0} = V_a\frac{\partial f_{m,ideal}}{\partial c_v}\bigg|_{c_v^0} \tag{17}$$

This leads to an expression for k_v^m,

$$k_v^m = \frac{1}{(c_v^0 - c_v^{m,eq})}\left[\frac{RT}{V_m}\left[\ln c_v^0 - \ln\left(1 - c_v^0\right)\right] + \frac{N_A E_v^f}{V_m}\right] \tag{18}$$

Here, for $c_v^0 = 0.01$, k_v^m varies linearly with temperature such that $k_v^m = 7335\,\mathrm{eV/nm^3} - 0.9682\,T\,\mathrm{eV/nm^3/K}$. The parabolic curvature for the the gas atoms is considered same as that of the vacancies.

Below 1200 K, the most mobile Xe defect is interstitial Xe [12]. Therefore, Xe and vacancy monomers arrive at the bubbles independently, unlike at higher temperatures where Xe-vacancy clusters are the most mobile Xe defect. Bubbles are created as vacancies first cluster together to provide space as voids in the UO_2 lattice, then these voids are filled by interstital Xe. Therefore, the bulk chemical free energy density of the gas bubble phase, f_b, is determined assuming that the bubbles are initially created as voids such that the equilibrium vacancy concentration within the bubble is $c_v^{b,min} = 1$. Any additional gas atoms that arrive at the bubble cause the bubble pressure to increase without changing the bubble size. Bubbles grow due to addition of vacancies to the bubble over time. This is different from the higher temperature cases simulated in earlier works, where the bubble phase is considered to be a mixture of U-site vacancies and Xe atoms as described in [11].

To simplify the numerical calculations, the Helmholtz free energy of the gas phase is also approximated utilizing a parabolic fit

$$f_b = \frac{1}{2}k_v^b(c_v - c_v^{b,min})^2 + \frac{1}{2}k_g^b(c_g - c_g^{b,min})^2 + f_0 \tag{19}$$

with $c_v^{b,min} = 1$ as described above. The value of k_v^b is set at 245 eV/nm^3, which was chosen to be large enough to keep c_v in the bubble close to 1, but small enough that it did not hinder numerical convergence of the simulations. The values of k_g^b, $c_g^{b,min}$, and f_0 were set by fitting a parabola to the Helmholtz free energy obtained from a virial equation of state (EOS) of Xe in UO_2 [13]. The Helmholtz free energy for the virial EOS is given by

$$f_g = c_g f_g^\circ + c_g\frac{kT}{V_a}\left[\ln\left(\frac{c_g}{c_g^\circ}\right) + \frac{B}{v_m}\frac{N_A}{\rho_g^c}(c_g - c_g^\circ) + \frac{C}{2v_m^2}\left(\frac{N_A}{\rho_g^c}\right)^2(c_g^2 - c_g^{\circ 2}) + \frac{E}{4v_m^4}\left(\frac{N_A}{\rho_g^c}\right)^4(c_g^4 - c_g^{\circ 4})\right] \tag{20}$$

where f_g° is the reference Helmholtz free energy of Xe per unit volume at reference molar volume v_g°, v_m is the molar volume of the gas, $c_g^\circ = v_m/v_g$, $v_m = 2.53 \times 10^{-5}$ m^3/mol is the molar volume of U sites in the solid, B, C, and E are temperature-dependent coefficients, and $\rho_g^c = 5.06$ nm^{-3} is the density of Xe atoms at the critical point. For all values of these parameters, please see Ref. [13, 14].

Plots of the Helmholtz free energy from the virial EOS, the van der Waals EOS, and the parabolic fit to the virial EOS are shown at 1000 K and 1050 K in Figure 1a and 1b, respectively. At 1000 K, $c_g^{b,min} = 1.0037$, $k_g^b = 6.33 \times 10^9$ J/m^3 or 39.51 eV/nm^3, and $f_0 = -3.10 \times 10^9$ J/m^3 or -19.36 eV/nm^3. At 1050 K, $c_g^{b,min} = 1.0080$, $k_g^b = 6.56 \times 10^9$ J/m^3 or 40.93 eV/nm^3, and $f_0 = -3.24 \times 10^9$ J/m^3 or -20.25 eV/nm^3.

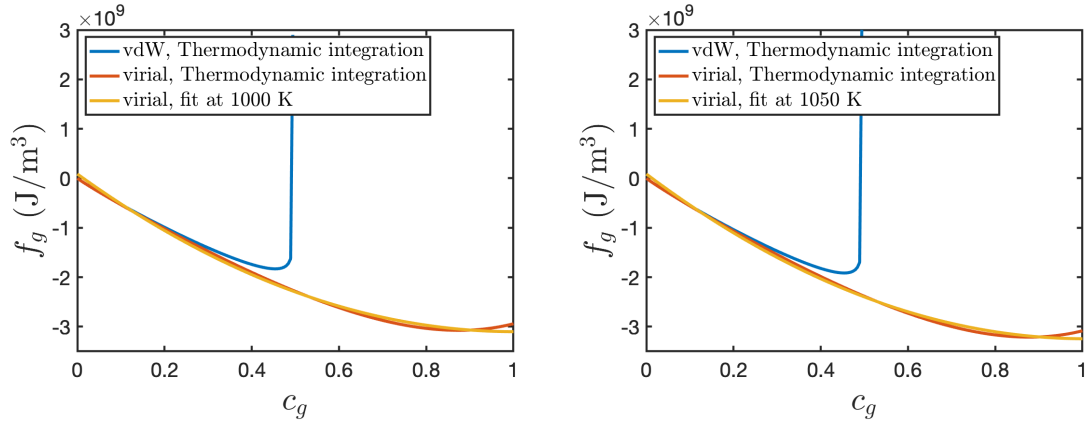

Figure 1. Gas phase Helmholtz free energy as a function of gas concentration at (a) 1000 K, (b) 1050 K.

2.3. Interfacial And Kinetic Parameters

In general, the grain boundary energy of UO_2 is considered to be $\sigma_{mm} = 1.5$ J/m^2 or 9.363 eV/nm^2. The interfacial energy between the matrix and gas bubble phase is considered to be same as the grain boundary energy, $\sigma_{mb} = \sigma_{mm}$. This results in a dihedral angle of 120° between the bubbles and the grain boundaries. The interfcial properties are calculated assuming interface thickness $l_{int} = 10$ nm. The free energy coefficients (in Equation 3, Equation 4) are obtained as [15]

$$\alpha = \frac{6\sigma_{mm}}{l_{int}}\,, \tag{21}$$

and

$$\kappa = \frac{3}{4}\sigma_{mm} l_{int}\,. \tag{22}$$

The kinetic mobility of the grains is obtained as

$$L_m = \frac{4M_{GB}}{3l_{GB}}, \tag{23}$$

where M_{GB} is the grain boundary mobility:

$$M_{GB} = M_0 \exp\left(-\frac{Q}{k_B T}\right)\,, \tag{24}$$

where $M_0 = 9.21 \times 10^{-9}$ m^4/Js, $Q = 3.01$ eV [16]. For the bubble-matrix interface, the kinetic mobility is defined such that the bubble evolution is solely diffusion controlled. To this end, the kinetic mobility of the

bubble phase is increased until the bubble evolution is not affected by the mobility value [17]. Based on this analysis, the kinetic mobility of the bubble phase is chosen as, $L_b = 10\, L_{GB}$.

The Xe diffusivity values are defined from the cluster dynamics simulations [18],

$$D_g = D_1(T) + D_2(T, \dot{F}) + D_3(\dot{F}) \tag{25}$$

$$D_1(T) = \frac{2.22 \times 10^{-7} \exp\left(-3.26/k_B T\right)}{1 + 29.0 \exp\left(-1.84/k_B T\right)} \tag{26}$$

$$D_2(T, \dot{F}) = 2.82 \times 10^{-22} \exp\left(-2.0/k_B T\right)\sqrt{\dot{F}} \tag{27}$$

$$D_3(\dot{F}) = 8.5 \times 10^{-40} \dot{F} \tag{28}$$

where D_g is in units of m^2/s. For typical LWR fission rate density of 1.09 $\times 10^{19}$ fissions/m^3-s and 1000 K temperature the gas diffusivity value is 9.35 $\times 10^{-3}$ nm^2/s. For the vacancy diffusion coefficients, we use the irradiation enhanced diffusivity value of 1.677 nm^2/s [19].

The Xe source term (in Equation 9) is calculated as:

$$s_g = \dot{F} y_{Xe} \tag{29}$$

where $\dot{F}$ is the fission rate and y_{Xe} = 0.2156, is the fission yield of Xe.

The vacancy source term is parameterized based on the approach described in Refs. [14] and [20]. Physically, both vacancies and interstitials are produced by collision cascades, and the kinetics of bubble growth are determined by the processes of defect production, vacancy-interstitial recombination, and absorption at sinks including dislocations and grain boundaries. Bubble growth results from preferential absorption of interstitials at dislocations, leading to a net excess of vacancies. In the present phase-field model that includes only vacancies, referred to as the source-only (SO) model, this can be represented by a net vacancy production rate s_v. The approach described in Refs. [14] and [20] allows the SO model to be parameterized through comparison with an analytical model that includes both vacancies and interstitials and their related kinetic processes in a simplified geometry, referred to as the chemical stress model [21].

In [20], for the SO model, an analytical expression for the radius R of a spherical void due to the vacancy source term in the surrounding solid matrix was derived for a spherical simulation domain with radius $\mathcal{R}$, assuming that the vacancy concentration in the matrix is in a quasi-steady state condition:

$$R = \left[s_v \mathcal{R}^3 t + R_0^3\right]^{1/3} \tag{30}$$

where t is the time, and R_0 is the initial radius of the bubble. For the chemical stress model, the radius as a function of time is given by

$$R = \left[2 D_v \left(1 - \frac{Z_v}{Z_i}\right) c_v^{ss} t + R_0^2\right]^{1/2} \tag{31}$$

where Z_v and Z_i are capture rates of the point defects by sinks such as dislocations, and c_v^{ss} is the steady-state concentration of vacancies in the matrix far from the void. The vacancy source strength s_v can be determined by finding the value that provides the best match between Equation 30 and 31. The exact values of Z_v are Z_i have not been determined for UO_2 to our knowledge, but Z_i is typically greater than Z_v by several percent [21]. Therefore, we assumed $Z_v = 1$ and considered the bounding cases $Z_i = 1.1$ and $Z_i = 1.02$. We then used a least-squares based optimization to find the values of s_v that give the best match between Equation 30 and 31 for typical simulation times.

Figures 2a and 2b show the results from this optimization for $Z_i = 1.1$ and $Z_i = 1.02$, respectively. Figure 2a also shows the results of a phase-field simulation performed in radial coordinates with spherical symmetry for comparison with the analytical solution; the results were in good agreement. We found that for $Z_i = 1.1$, $s_v = 15.9 s_g$ provided the best match, while for $Z_i = 1.02$, $s_v = 1.94 s_g$ provided the best match. Therefore, $s_v = 10 s_g$ was chosen as a reasonable intermediate value between the bounding cases since the exact values of Z_v are Z_i are not known.

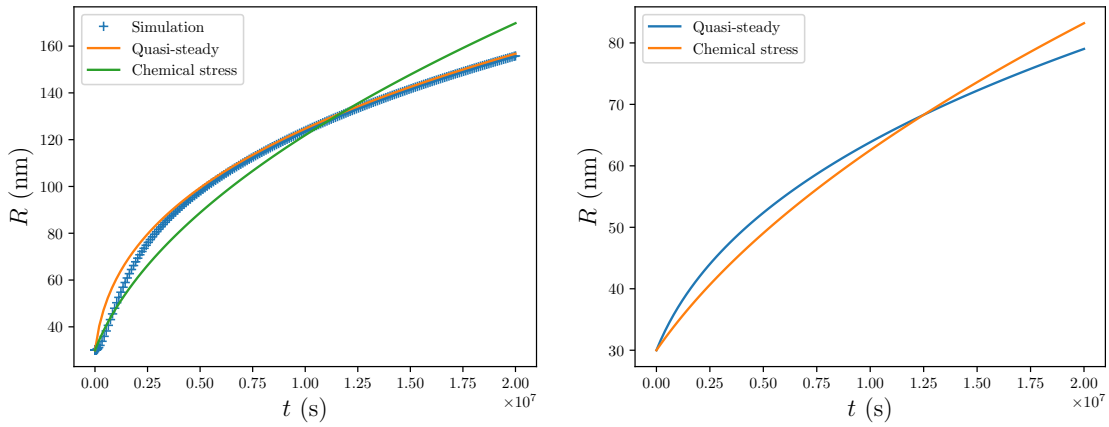

(a) (b)

Figure 2. Comparison between predictions for bubble radius versus time using the analytical expression for the SO model in the quasi-steady state limit (Equation 30) and the chemical stress model (Equation 31). (a) assumes $Z_i = 1.1$ and (b) assumes $Z_i = 1.02$. Simulation results using a phase-field model in (a) show good agreement with the quasi-steady state approximation.

2.4. Restructuring Criteria

In the present phase-field model, the restructuring of the grains is modeled as subgrain formation via dynamic recrystallization using a discrete nucleation algorithm. Previously, a restructuring model was developed for HBS which used a dislocation density-based nucleation criteria such that nucleation occurs when effective dislocation density exceeds the critical dislocation density for restructuring. For the dark zone, we updated the model to include a energy balance-based criteria following the work proposed by Takaki et al. [22]. In this case, we assume that restructuring occurs when the dislocation energy, defined in Equation 6, is higher than the energy penalty for forming a new subgrain. The dislocation density (d_i) within a grain is defined following an empirical correlation derived based on experimental observation [23] such that

$$\log_{10} d_i = 2.2 \times 10^{-2} \beta + 13.8, \tag{32}$$

where β is the burnup in GWd/tU. Note that this correlates the pellet average burnup to the dislocation densities. We use the same correlation to calculate the dislocation density in the dark zone by substituting average burnup with local effective burnup. Here, the local effective burnup (β_{eff}) is defined as:

$$\beta_{eff} = k_\beta \left(t - t_0\right) , \tag{33}$$

where k_β is the burnup rate in GWd/tU/s, t is current time, and t_0 is the initial time when a grain or subgrain is formed. Considering that dislocation densities within a grain can very depending on its crystallographic orientation, the initial dislocation densities (d_{i0}) within different grains are assigned randomly such that

$$d_{i0} = R\, d_0 , \tag{34}$$

where R is a random value in [0, 1] and d_0 is the specified constant dislocation density. The effective dislocation density is calculated as:

$$d_{eff} = \frac{\sum_{i=1}^{n_m} d_i \eta_{mi}^2}{\sum_{i=1}^{n_m} \eta_{mi}^2} , \tag{35}$$

where d_i is the dislocation density within a grain. When a new subgrain is formed, the dislocation density within that subgrain is set to a lower value of 1×10^{-5} nm/nm^3, assuming that subgrain formation occurs due to the organization of dislocations into grain boundaries surrounding the nano-scale regions of defect-free material. This value is set such that it is below the dislocation density value at zero burnup according to Equation 32.

The subgrain formation energy is defined as

$$E_{sub} = k_s \gamma / D \tag{36}$$

where γ is the interface energy (considered to be the same as the GB energy), D is the subgrain diameter, and k_s is a dimensionless geometrical factor for subgrain formation. Restructuring occurs via formation of new subgrains, when $\omega_d > E_{sub}$. The value of k_s in Equation 36 is set such that the subgrain formation based on the energy-based restructuring criteria begins at a threshold burnup consistent with experimental observations. Figure 3 shows the evolution of dislocation density and corresponding energy density with burnup. Subgrain formation energy for a 200 nm radius subgrain is overlaid to demonstrate the energy-based restructuring criteria. Assuming a subgrain radius of 200 nm and setting $k_s = 1.0$, the restructuring would begin above threshold burnup of 40 GWd/tU. This matches the experimental observations [3].

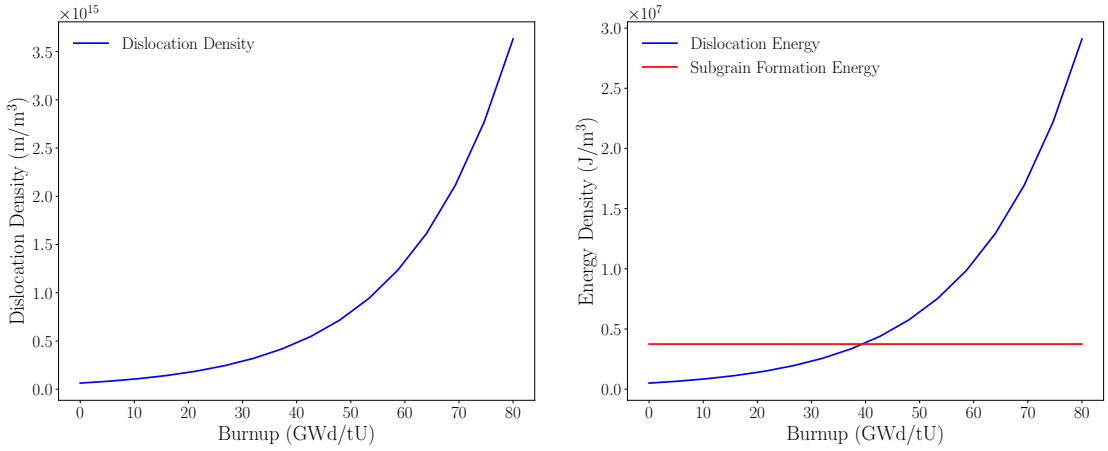

(a) (b)

Figure 3. Evolution of (a) dislocation density (Equation 32) and (b) dislocation energy density (Equation 6) within the fuel as a function of burnup.

The new subgrains are introduced utilizing a discrete nucleation method where nuclei of a finite size are introduced in a stochastic fashion once the energy-based restructuring criteria is met. A simple linear relationship is employed to define the subgrain formation rate, $\dot{n}$,

$$\dot{n} = \langle \eta_i \eta_j \rangle \, k_d d_{eff}, \tag{37}$$

where k_d is the nucleation rate prefactor indicating the fraction of the local dislocation density that contributes to the subgrain formation. Here, the function $\langle \eta_i \eta_j \rangle$ is defined as

$$\langle \eta_i \eta_j \rangle = 1, \text{ for } \eta_i \eta_j > \eta_{crit} \tag{38}$$

$$= 0, \text{ otherwise} \tag{39}$$

The value for η_{crit} is considered to be 0.75. The term $\langle \eta_i \eta_j \rangle$ ensures that the new subgrains are formed around the grain boundaries of the existing grains and bubble surfaces. Furthermore, a nucleation bias is included for

the bubble surfaces. Considering bubbles provide a free surface as a sink for dislocations, the energy penalty for creating a subgrain around bubble is reduced. Depending on the subgrain shape, the bubble surface covers a fraction of the subgrain boundary. Assuming only one segment of the subgrain boundary coincides with the bubble surfaces, the coverage fraction could be $1/6$ for a hexagonal grain. Whereas, for a circular grain the coverage fraction could be as high has $1/2$. For any other arbitrary grain shapes the coverage fraction could vary. Based-on this, the geometric factor for the subgrain energy in Equation 36 is modified such that:

$$k_s = r_b k_{s0}, \text{for } \eta_b > 0.01 \tag{40}$$

$$= k_{s0}, \text{otherwise} \tag{41}$$

We set $k_{s0} = 1.0$ and $r_b = 0.5$ to evaluate the effect of this local reduction in E_{sub} on the nucleation probability and restructuring fraction. The local nucleation probability, $P(r)$, is defined as

$$P(r) = v\,\dot{n}, \tag{42}$$

where v is the volume over which the local subgrain formation rate is being integrated. A Bernoulli trial is performed to determine if a nucleus is introduced by comparing a random value R in [0, 1] against P. If $R < P$, a nucleus is introduced at that location.

The burnup and temperature values for the simulations are chosen based on experimental observations. Figure 4 shows the burnup and temperature profile across radial direction of the fuel. We use this to calibrate the subgrain formation parameters for the dark zone. The baseline simulation parameters for 1000 K temperature are listed in Table 1. Any deviation from these values will be mentioned while describing the corresponding simulations in Section 3.

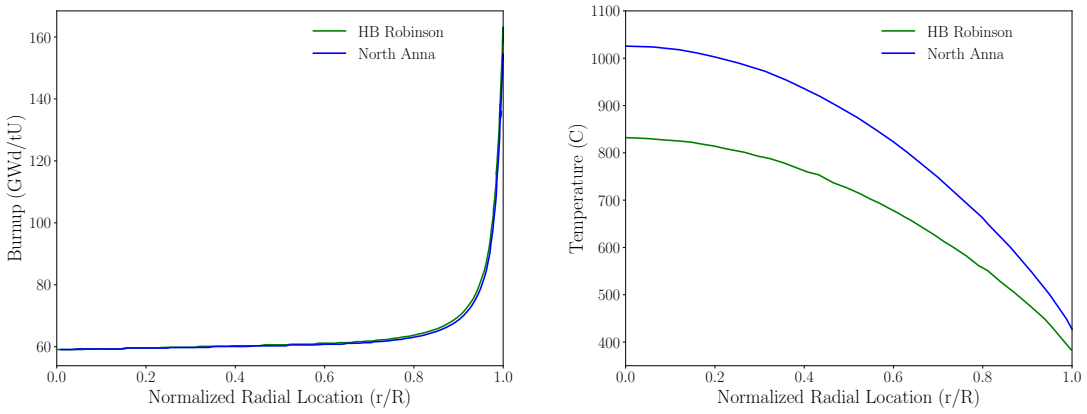

(a) (b)

Figure 4. Comparison of fuel burnup and temperature variations across radial direction observed in experiments (reproduced from [1] using Plotdigitizer [2]).

2.5. Computational Details

For implementation and numerical solution of the current model, we utilize the open-source parallel MOOSE framework and MOOSE-based application, MARMOT. For the 2D simulations presented here, the finite element meshes are comprised of four-node quadrilateral elements (QUAD4). Meshes are generated with the internal MOOSE mesh generator and linear Lagrange shape functions are used for all the nonlinear

Parameter	Formulation	Value	Source
T		1000 K	
$\dot{F}$		1.09×10^{19} fission/m^3/s	
V_a		0.04092 nm^3	[24]
E_f^v		3 eV	[11]
E_f^g		3 eV	[11]
$c_{v/g}^{m,eq}$	$\exp\left(-\frac{E_v^f}{k_B T}\right)$	2.515×10^{-13}	[17]
k_v^m/k_g^m	$7335\,\text{eV/nm}^3 - 0.9682\,T\,\text{eV/nm}^3/\text{K}$	6366.8 eV/nm^3	[17]
$c_v^{b,eq}$		1.0	[17]
$c_g^{b,eq}$		1.0037	[17]
k_v^b		245 eV/nm^3	[17]
$k_{v/g}^b$		39.51 eV/nm^3	[17]
f_0		-19.36 eV/nm^3	[17]
l_{int}		10 nm	
σ_{mm}		1.5 J/m^2 or 9.363 eV/nm^2	
κ	$\frac{3}{4}\sigma_{mm} l_{int}$	1.125×10^{-8} J/m or 70.2 eV/nm	[17]
α	$\frac{6\sigma_{mm}}{l_{int}}$	9×10^8 J/m^3 or 5.62 eV/nm^3	[17]
γ_{mm}/γ_{mb}		1.5	
G		64.1 GPa	[25]
b_g		$5 \times 10^{-10} m$	
M_{GB}	$9.21 \times 10^{-9} \exp\left(-\frac{3.01}{k_B T}\right)$ m^4/Js	1.62×10^{-5} nm^4/eV/s	[17]
L_{GB}	$\frac{4M_{GB}}{3l_{int}}$	2.16×10^{-6} nm^3/eV/s	[17]
L_b	$10 L_{GB}$	4.58×10^{-4} nm^3/eV/s	[26]
s_g	$\dot{F} y_{Xe}$	2.35×10^{-9} atoms/(nm^3 s)	[26]
s_v	$10 s_g$	2.35×10^{-8} atoms/(nm^3 s)	[26]
D_g^m		9.351×10^{-3} nm^2/s	[26]
D_v^m		1.67 nm^2/s	[26]

Table 1. Parameters used for phase-field simulations of dark zone formation.

variables. The system of nonlinear equations is solved with the preconditioned Jacobian Free Newton-Krylov (PJFNK) [27] method. We employ the additive Schwarz method (ASM) for preconditioning and iterative LU factorization for sub-preconditioning. The simulations are solved with a linear tolerance of 1×10^{-3}, nonlinear relative tolerance of 1×10^{-6}, and a nonlinear absolute tolerance of 1×10^{-8}. Automatic residual scaling is utilized to minimize any disparities in the residual norms corresponding to different nonlinear variables. For the time integration, implicit time integration scheme with second order backward differentiation formula (BDF2) is employed. Furthermore, adaptive meshing and time stepping schemes are used to reduce the computational cost. The mesh is refined around the interface and coarsened in the other areas. This is achieved by refining the mesh in regions of high curvature in the order parameter fields with the help of a gradient jump indicator scheme [28] within MOOSE. This adaptive meshing scheme allows us to appropriately resolve the interface without significantly increasing the computational cost. Additionally, an iteration-based time adaptivity scheme is employed to increase the time step, based on the number of iterations required to solve the coupled equation system. The optimal iteration window of 6 ± 1 is adopted. Periodic boundary conditions are used to eliminate any boundary effect on the solution.

3. RESULTS AND DISCUSSION

A simulation domain with $12.5\ \mu m \times 12.5\ \mu m$ size was initialized with 4 grains and a single 100 nm radius bubble. Average grain diameter at the beginning of the simulation is 7 μm. We start the simulations assuming that the initial grains are somewhat damaged and have accumulated a certain amount of dislocations (exact values specified in the following sections). Considering the temperature bounds for the dark zones, simulations are performed at 1000 K and 1050 K temperatures. Since the physical value of some of the parameters needed for the restructuring model are not available in the literature, we systematically vary the modeling parameters and evaluate how each of those parameters influence the restructuring behavior.

3.1. Effect Of Subgrain Formation Parameters

For the first set of simulations, we initialize the dislocation densities within the grains ensuring that the maximum dislocation density of 6×10^{-4} nm/nm^3 is achieved in one of the grains. This assigns the initial dislocation densities within the grains slightly below the threshold value for restructuring. This represents an initial burnup around 44.5 GWd/tU. These simulations are run at 1000 K temperature. Burnup rate (k_β in Equation 33) and nucleation rate prefector for subgrain formation (k_d in Equation 37) are varied to evaluate the role of subgrain formation rate and identify appropriate parameters corresponding to the dark zone. Nogita and Une [23] reported that above 44 GWd/tU, the dislocation density seems to be saturated ((5-6) $\times 10^{14}$ m/m^3). We hypothesize that this is primarily due to the initiation of restructuring that converts dislocation networks into subgrain boundaries. However, within the damaged regions of the original grains further dislocation accumulation is possible due to continuous increase in burnup. Hence, we simulate two restructuring scenarios with different burnup rates. In the other scenario, we consider the effect of a higher nucleation rate prefactor. The details about the subgrain formation parameters used in different simulations are provided in Table 2.

Parameters	Case I	Case II	Case III
Burnup Rate, k_β (GWd/tU/s)	4.2654×10^{-7}	4.2654×10^{-7}	4.2654×10^{-6}
Nucleation Rate Prefactor, k_d	8.5×10^{-3}	1×10^{-3}	1×10^{-3}
Initial Subgrain Formation Rate, $\dot{n}$	5.3×10^{-5}	6.2×10^{-6}	6.2×10^{-6}

Table 2. Subgrain formation parameters used in phase-field simulations for dark zone formation at 1000K temperature.

Figure 5 to Figure 7 shows the restructuring observed in the three cases presented in Table 2, respectively. It is observed that restructuring occurs in two stages: formation of new subgrains followed by the coarsening of the subgrains. Comparing Case I and Case II, it is noticed that lower subgrain formation rate in Case II allows for more coarsening to occur. Thus, the average grain diameter in Case II is higher than Case I. Furthermore, the initial dislocation densities within the grains are assigned randomly around a specified constant value, following Equation 32. The specified value of d_{i0} in Equation 32 is chosen to ensure that the dislocation densities within the grains are close to the threshold value for restructuring. This process can assign dislocation densities below what is necessary for subgrain formation. Thus, only two of the four initial grains meet the subgrain formation criteria at the initial condition. This results in a local restructuring bias as observed within the simulated microstructure for Case I and Case II. Here, restructuring bias refers to the difference in the probability of subgrain formation among different grains or regions of the microstructures. For example, as observed in Figure 5c, only one grain is fully restructured at 58.6 GWd/tU burnup.

Comparing Case II and Case III, it is observed that even though both the cases had same initial subgrain formation rate, grain morphologies for both the cases vary significantly. For Case III, higher burnup rate results is a sharp increase in the effective dislocation densities which increases the subgrain formation rate as the simulation progresses. Thus, a sharp increase in number of subgrain is observed in case III. Moreover, the grains which initially had dislocation densities below the threshold value for subgrain formation, quickly reach high enough burnup and accumulate enough dislocations to induce restructuring. Microstructures corresponding to case III reach very high burnup due to the high burnup rate used in the simulation. Thus, Case III is more representative of the peripheral regions, rather than the dark zone. Figure 8 compares the evolution of number of grains and average grain diameter among the three cases presented in Table 2. Number of grains increase and average grain diameter decreases during the subgrain formation stage. During the coarsening stage, average grain diameter increases. In general, the number of subgrains increase and average grain diameters decrease with increase in subgrain formation rate. Subgrain formation rate is influenced by the combination of nucleation rate prefactor and burnup rate, which determines the change in dislocation density. Higher subgrain formation rate, however, results in less coarsening and more new subgrain formation. Average grain diameter in the restructured fuel varies between $1\ \mu m$ and $2.5\ \mu m$.

3.2. Effect Of Dislocation Densities

For Case IV, we increase the initial dislocation densities within the grains. In this case, the initial dislocation density is set around a maximum value of 7.33×10^{-4} nm/nm^3 and the nucleation rate prefactor k_d used is 9.0×10^{-4}. This results in an initial subgrain formation rate of 6.5×10^{-6}. All other simulation parameters remains the same as in Case II presented in Section 3.1. The relevant simulation parameters are compared in Table 3. Figure 9 shows the different restructuring stages for Case IV. It is notable that the initial dislocation densities within all the grains are high enough to induce restructuring without any localized subgrain formation preference or bias. Higher initial dislocation density results in higher subgrain formation rate leading to faster restructuring.

Figure 10 compares the evolution of number of grains and average grain diameter with time between Case

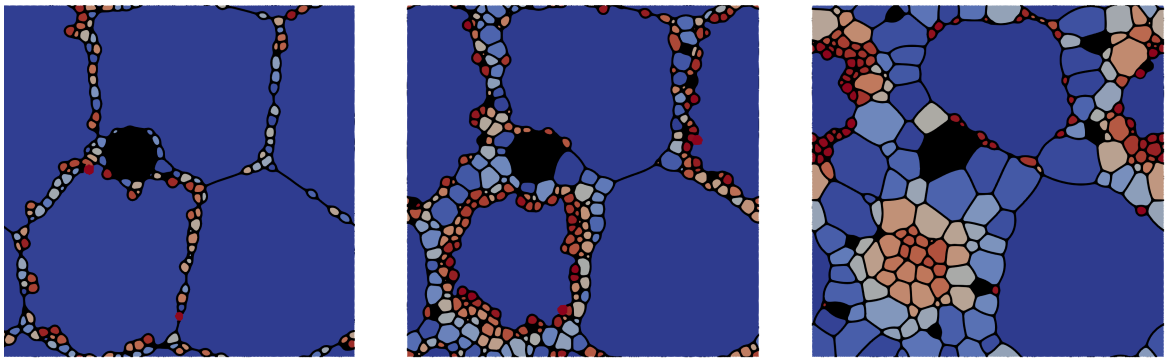

(a) (b) (c)

Figure 5. Different restructuring stages simulated at 1000K temperature for Case I at (a) 1.86×10^6 sec (b) 1.0×10^7 sec (c) 3.3×10^7 sec. Corresponding restructuring fractions are 9.42% at 45.2 GWd/tU, 26.87% at 48.7 GWd/tU, and 60.74% at 58.6 GWd/tU, respectively.

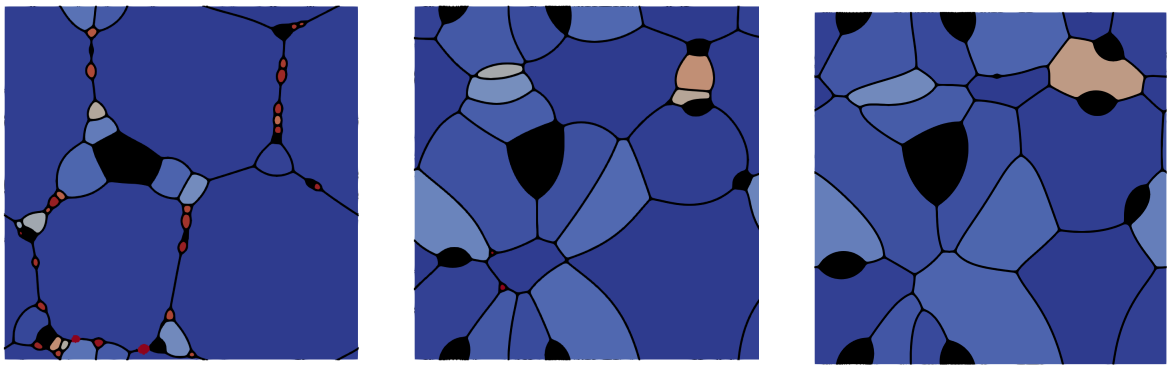

(a) (b) (c)

Figure 6. Different restructuring stages simulated at 1000K temperature for Case II at (a) 2.65×10^7 sec (b) 7.12×10^7 sec (c) 1.0×10^8 sec . Corresponding restructuring fractions are 12.23% at 55.7 GWd/tU, 52.88% at 74.8 GWd/tU, and 85.47% at 87.1 GWd/tU, respectively.

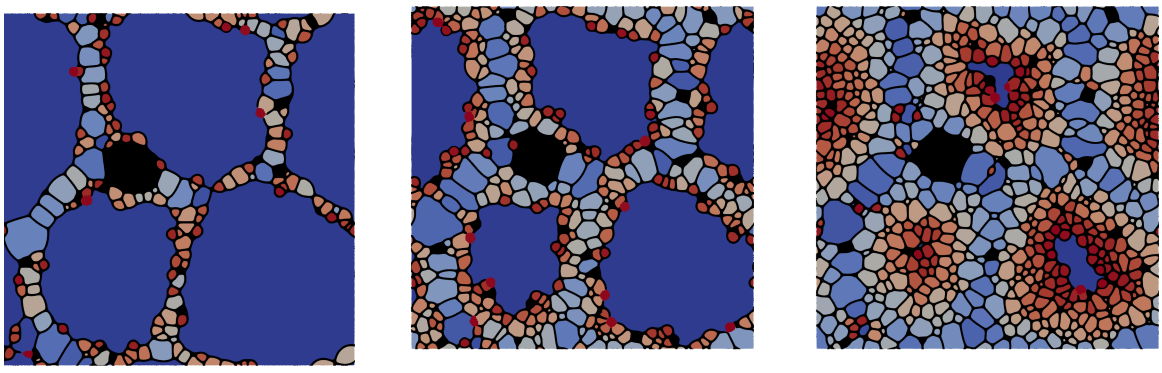

(a) (b) (c)

Figure 7. Different restructuring stages simulated at 1000K temperature for Case III at (a) 2.15×10^7 sec (b) 2.55×10^7 sec (c) 2.92×10^7 sec. Corresponding restructuring fractions are 27.23%, 54.37%, and 98.71% respectively.

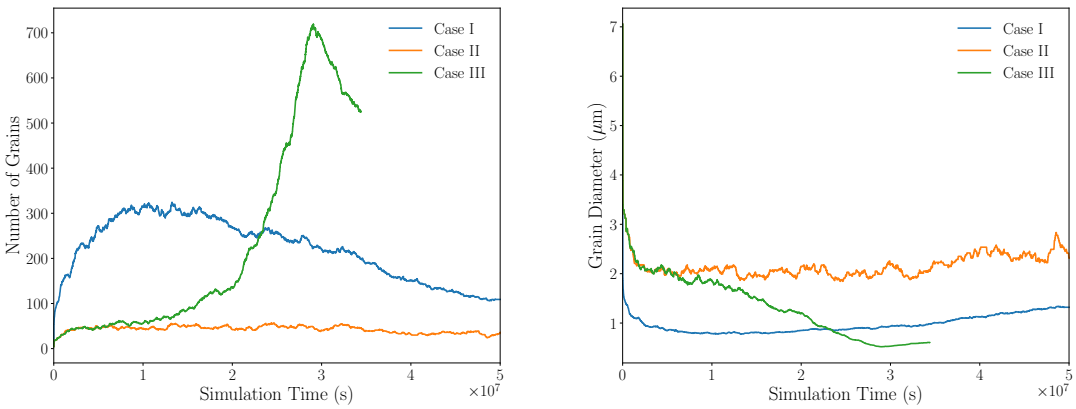

(a) (b)

Figure 8. Evolution of (a) number of grains and (b) average grain diameter with time for the three cases presented in Table 2.

II and Case IV. These two cases had different initial dislocation densities (d_{i0}), but similar nucleation rate prefactors (k_d). Although the initial subgrain formation rates are similar, the subgrain formation rate continues to be high for much longer for Case IV because there are more locations available for subgrain formation to begin (since restructuring can occur in all grains at the start of the simulation in Case IV). Changes in initial dislocation density not only change the subgrain formation rate, but also influence the restructuring bias observed among different grains. Thus, it plays an important role in dictating the characteristics of the restructured fuel regions. With increase in initial dislocation densities, restructuring occurs significantly faster. Additionally, the continued high subgrain formation rate in Case IV also results in smaller average grain size.

Parameters	Case II	Case IV	Case V
Initial Dislocation Densities, d_{i0} (nm/nm^3)	6.0×10^{-4}	7.33×10^{-4}	5.0×10^{-4}
Initial Subgrain Formation Rate, $\dot{n}$	6.2×10^{-6}	6.5×10^{-6}	4.4×10^{-6}

Table 3. Different initial dislocation densities used for phase-field simulations of dark zone formation at 1000 K temperature.

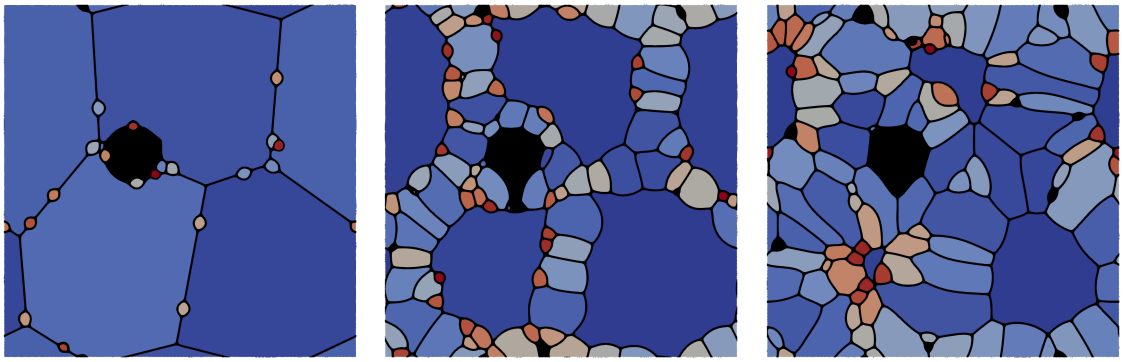

(a) (b) (c)

Figure 9. Different restructuring stages simulated at 1000K temperature for Case IV at (a) 2.09×10^7 sec (b) 2.85×10^7 sec (c) 3.7×10^7 sec. Corresponding restructuring fractions are 3.46% at 45.7 GWd/tU , 49.99% at 48.6 GWd/tU, and 96.79% at 52.1 GWd/tU, respectively.

3.3. Effect Of Bubble Distribution

For the next case, Case V, we initialize the domain with 6 bubbles having 60 nm radius. The nominal value of initial dislocation density is set at 5.0×10^{-4} nm/nm^3 and the prefactor for nucleation rate used is 9.0×10^{-4}. This results in an initial subgrain formation rate of 4.4×10^{-6}. All other simulation parameters are the same as in Case I presented before. Figure 11 shows the different restructuring stages for this case. It is observed that the subgrain formation initiates around the existing bubbles even when the dislocation densities within the grain have not reached the critical values for restructuring. This primarily happens due to the lower energy barriers for subgrain formation around the bubbles as compared to the grain boundaries. Additionally, although it is not considered in the present model, dislocation punching around the bubbles may also play a role by inducing higher localized damage around the bubbles and thus facilitating subgrain formation; this effect will be considered in future work. Similar to the previous cases, subgrain formation is

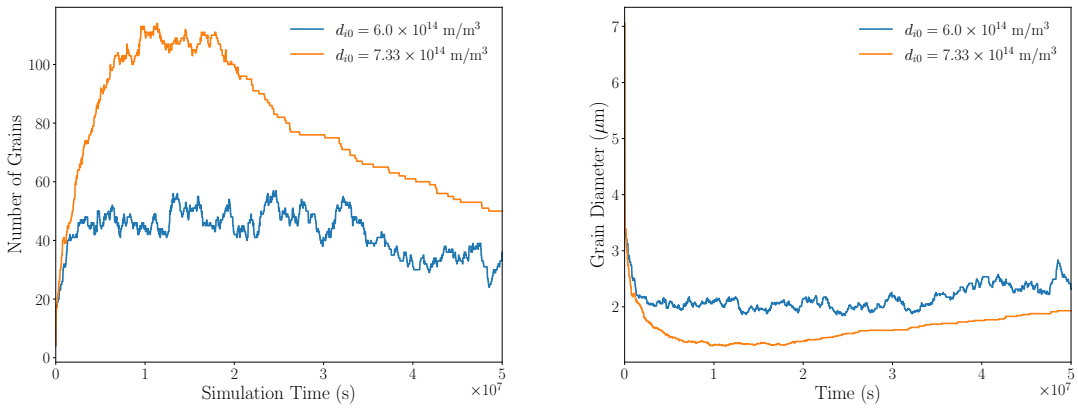

(a) (b)

Figure 10. Evolution of (a) number of grains and (b) average grain diameter with time for different initial dislocation densities corresponding to Cases II and IV reported in Table 3.

followed by a coarsening stage. It is noteworthy that even though restructuring initiates around the existing bubbles, bubble size distribution does not seem to influence the rate of restructuring.

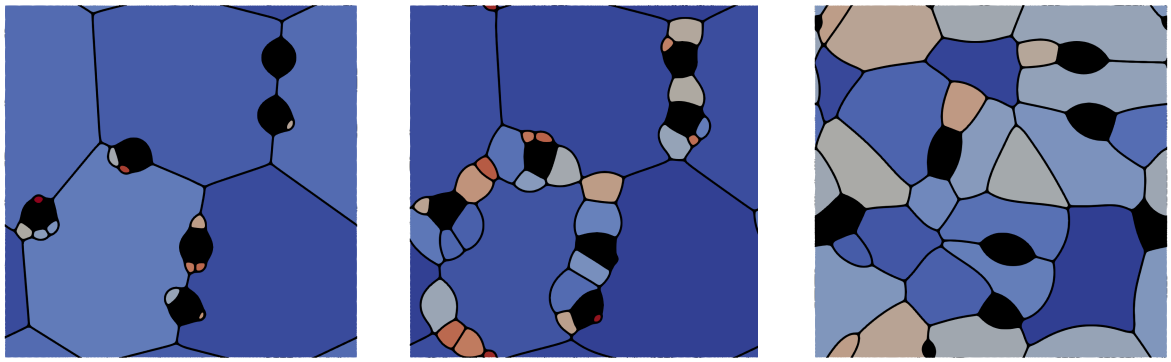

(a) (b) (c)

Figure 11. Different restructuring stages simulated at 1000 K temperature for Case V at (a) 1.66×10^6 sec (b) 9.41×10^6 sec (c) 3.35×10^7 sec. Corresponding restructuring fractions are 5.89% at 41.6 GWd/tU , 15.64% at 44.8 GWd/tU, and 85.58% at 55.1 GWd/tU, respectively.

3.4. Effect Of Temperature

Next, we simulate the restructuring at 1050 K temperature with varying dislocation densities and subgrain formation rates. The parameter values are reported in Table 4. Figure 12 and Figure 13 present different restructuring stages for the two cases presented in Table 4. Higher temperature facilitates defect annihilation and coarsening of the subgrains. Thus, the restructuring occurs faster at higher temperature.

Parameters	Case VI	Case VII
Initial Dislocation Densities, d_{i0} (nm/nm^3)	6.0×10^{-4}	5.0×10^{-4}
Initial Subgrain Formation Rate, $\dot{n}$	5.3×10^{-5}	1.5×10^{-5}

Table 4. Parameters used for phase-field simulations of dark zone formation at 1050 K.

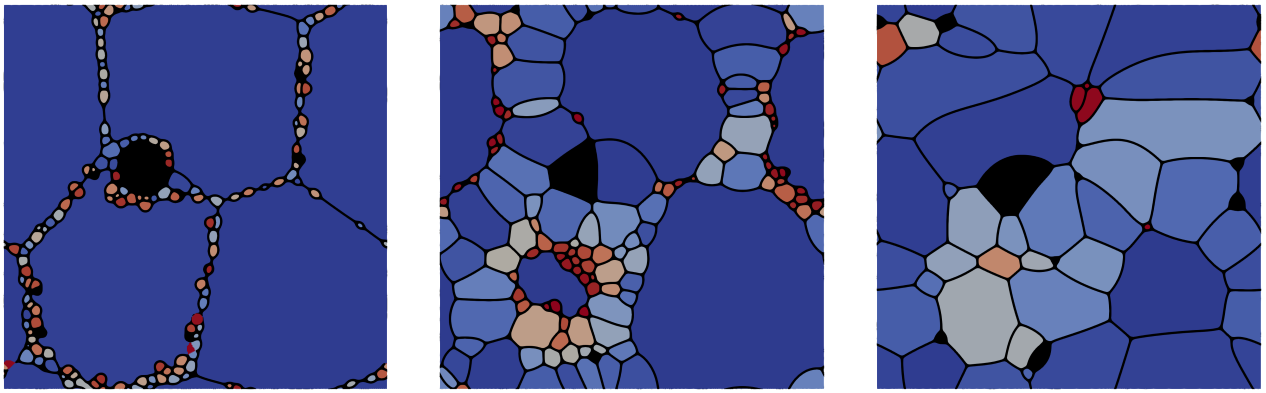

(a) (b) (c)

Figure 12. Different restructuring stages simulated at 1050K temperature for Case VI at (a) 6.77×10^5 sec (b) 7.84×10^6 sec (c) 2.16×10^7 sec. Corresponding restructuring fractions are 9.6% at 44.75 GWd/tU , 49.05% at 47.8 GWd/tU, and 93.31% at 53.7 GWd/tU, respectively.

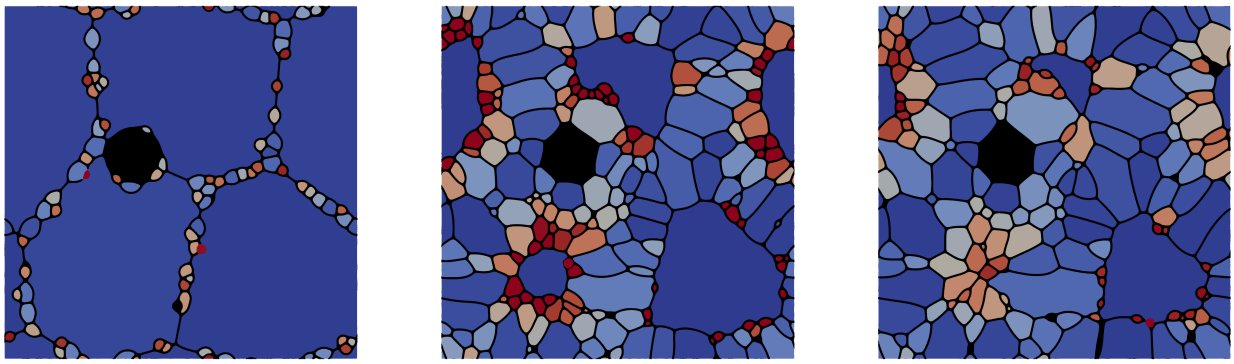

(a) (b) (c)

Figure 13. Different restructuring stages simulated at 1050 K temperature for Case VII at (a) 4.6×10^5 sec (b) 4.2×10^6 sec (c) 3.35×10^7 sec. Corresponding restructuring fractions are 10.34% at 44.6 GWd/tU , 76.98% at 46.2 GWd/tU, and 90.52% at 46.9 GWd/tU, respectively.

3.5. Analysis Of The Restructured Fuel

In this section, we analyze all the cases presented in Section 3.1 through Section 3.4 together to assimilate the combined effect of subgrain formation rate and temperature on the restructuring behavior. Figure 14

depicts the evolution of number of grains and average grain diameter with time for different subgrain formation rates at 1000 K temperature. The data presented here are from Case I, Case, II, Case IV and Case V. Different subgrain formation rates result from varying the initial dislocation densities and the nucleation rate prefactor. With increase in subgrain formation rate, the number of grains increases quickly. Average grain size also reduces with increase in subgrain formation rate. Figure 15 compares the evolution of number of grains and average grain diameter for different temperatures with a subgrain formation rates of 5.3×10^{-5} (Case I vs. Case IV). It is observed that the rate of restructuring and average grain size increases with increase in temperature. For the same subgrain formation rate, restructuring happens faster and average grain diameter is larger at higher temperature.

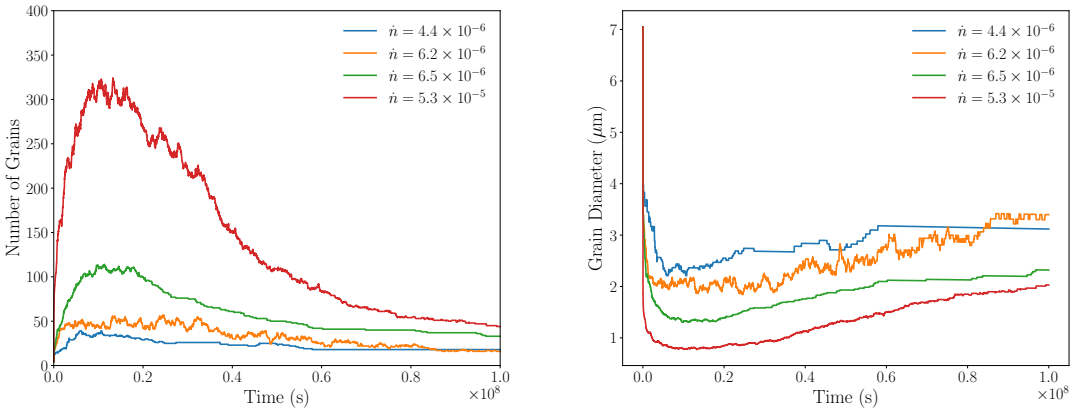

(a) (b)

Figure 14. Evolution of (a) number of grains, and (b) average grain diameter at 1000 K temperature with time for different subgrain formation rates. Different subgrain formation rates are obtained by varying the initial dislocation densities and nucleation rate prefactor.

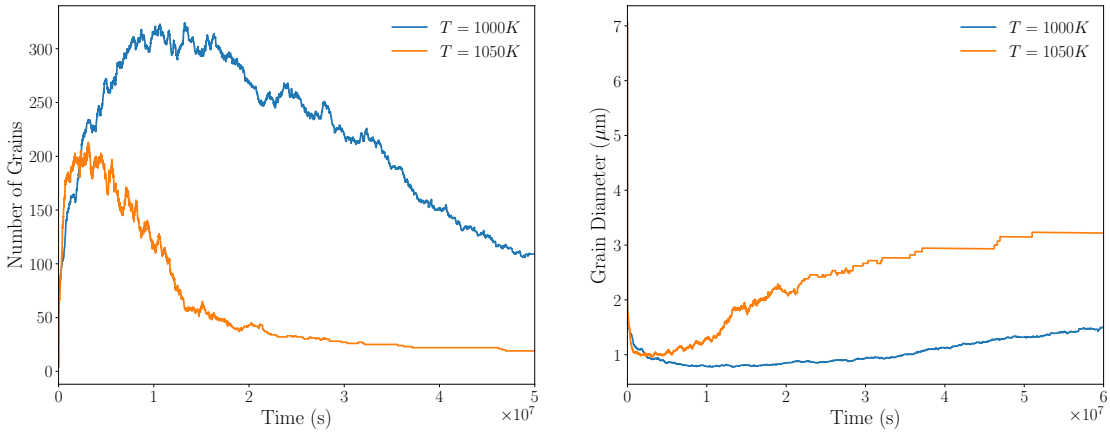

(a) (b)

Figure 15. Evolution of (a) number of grains and (b) average grain diameter with time for different temperatures with initial subgrain formation rate of 5.3×10^{-5}.

Figure 16 depicts the evolution of the volume fraction of restructured fuel as a function of local effective burnup for a combination of different nucleation rates and different temperatures. In general, the restructured volume fraction can be fitted using the Johnson-Mehl-Avrami-Kolmogorov (JMAK) correlation for phase transformations such that [29]:

$$\alpha = 1 - \exp\left(-k\,\beta_{eff}^{n}\right) \tag{43}$$

where α is the volume fraction of the new subgrains, k is the transformation rate constant, β_{eff} is the effective burnup, and n is the Avrami constant. Here, we fit a modified JMAK correlation such that

$$\alpha = 1 - \exp\left[-k\ \left(\beta_{eff} - \beta_{th}\right)^{n}\right]\ , \tag{44}$$

where β_{th} is the threshold burnup beyond which restructuring is observed. Based on the restructuring criteria described in Figure 3, the threshold burnup is taken as 40 GWd/tU. The fitting parameters corresponding to different combination of subgrain formation rates and temperatures are provided in Table 5. It is observed that rate of restructuring increases with increase in subgrain formation rate prefactor as well as temperature (Figure 16a and Figure 16c). For the same subgrain formation rate, restructuring occurs faster at higher temperature. This primarily happens due to the subgrain coarsening at higher temperature. As also observed in Figure 15, more subgrains are created at 1000 K temperature as compared to 1050 K. However, higher temperature allows for more coarsening that follows the subgrain formation. Thus, the restructuring progresses faster at higher temperatures. Changes in initial dislocation density significantly shift the restructuring curve. For the same nucleation prefactor, restructuring happens faster at higher initial dislocation densities.

Simulations	Temperature (K)	Initial Dislocation Density (nm/nm^3)	Initial Subgrain Formation Rate	Transformation Rate Constant (k)	Avrami Constant (n)
Case V	1000	5.0×10^{-4}	4.4×10^{-6}	5.905×10^{-3}	2.13
Case II	1000	6.0×10^{-4}	6.2×10^{-6}	8.152×10^{-5}	2.59
Case IV	1000	7.33×10^{-4}	6.5×10^{-6}	2.268×10^{-8}	6.96
Case I	1000	6.0×10^{-4}	5.3×10^{-5}	1.044×10^{-2}	1.51
Case VII	1050	6.0×10^{-4}	5.3×10^{-5}	1.127×10^{-3}	3.04
Case VI	1050	5.0×10^{-4}	1.5×10^{-5}	9.827×10^{-7}	7.79

Table 5. Simulation details and JMAK fitting parameters for the cases presented in Figure 16.

3.6. Comparison With Experimental Data

Figure 17 shows a sample dark zone microstructure [3] and grain size variation across the radial direction of the fuel observed in different restructured fuels [1]. In the case of North Anna fuel, grain size decreases radially with a sharp decrease in grain size observed around radial position 0.55. Temperature at that location is around 1120 K. For the HB Robinson (HBR) fuel the sharp decrease in grain size is observed around 0.4. Gerczak et al. [3] concluded that the dark zone is observed from 0.35-0.45 radial location. Corresponding temperatures at those radial positions are 1000 K and 1050 K (see Figure 4). Thus, phase field simulations were performed at those temperatures. Analysis for other temperatures will be performed in the future. BISON currently does not have any restructuring model for the dark zone. Hence, it fails to predict any grain size reduction (Figure 17b). The current mesoscale work aims to provide a mechanistic restructuring model that BISON can use to improve its predictions for validation purposes. The average grain diameter reported in the dark zone are 3.6 μm and 6 μm for the HBR and North Anna fuel, respectively (see Figure 17b).

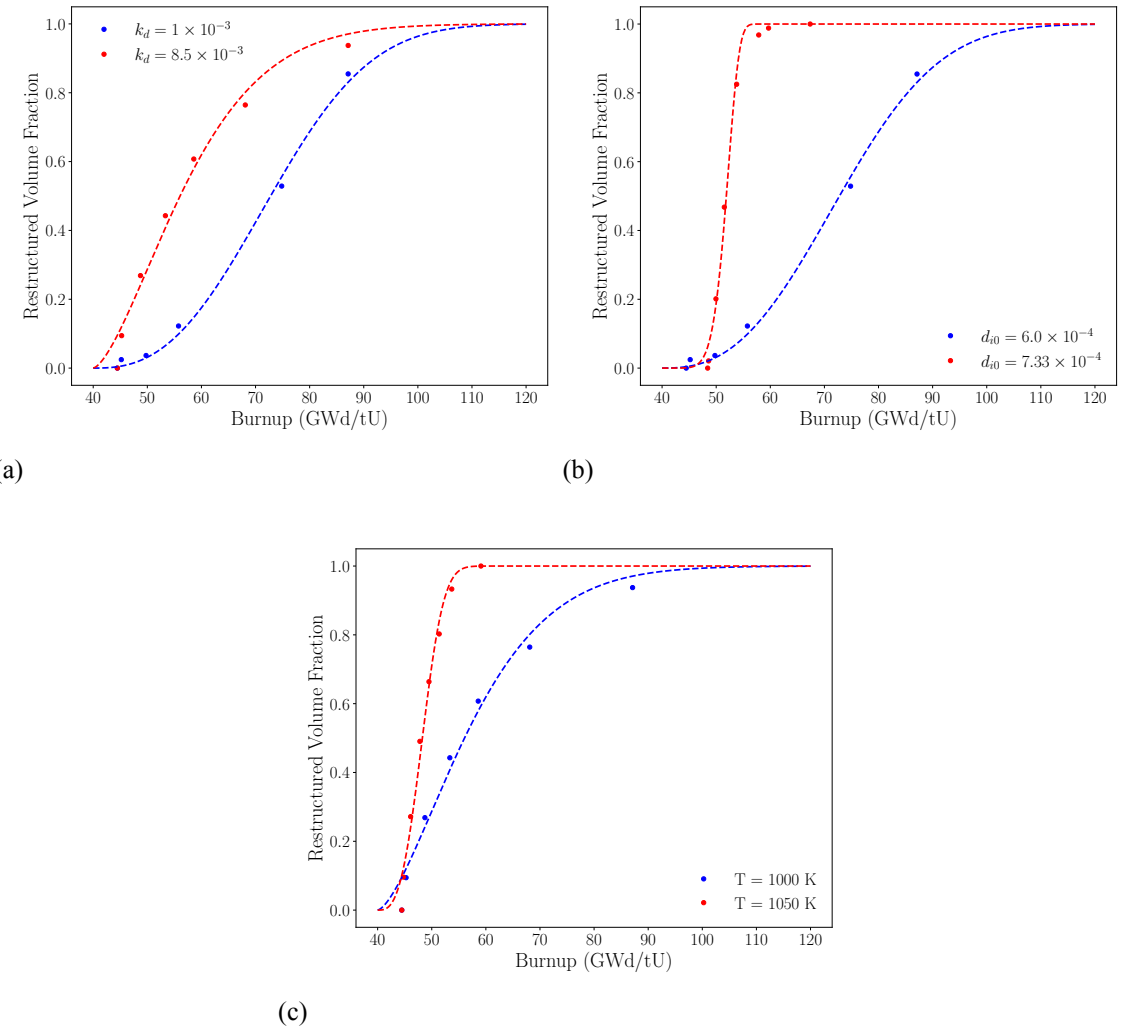

Figure 16. Volume fraction of restructured fuel and fitted JMAK relationship as a function of local effective burnup for (a) different nucleation rates prefactor, (b) different initial dislocation densities at 1000 K temperatures and (c) different temperatures. The corresponding fitting parameters are listed in Table 5

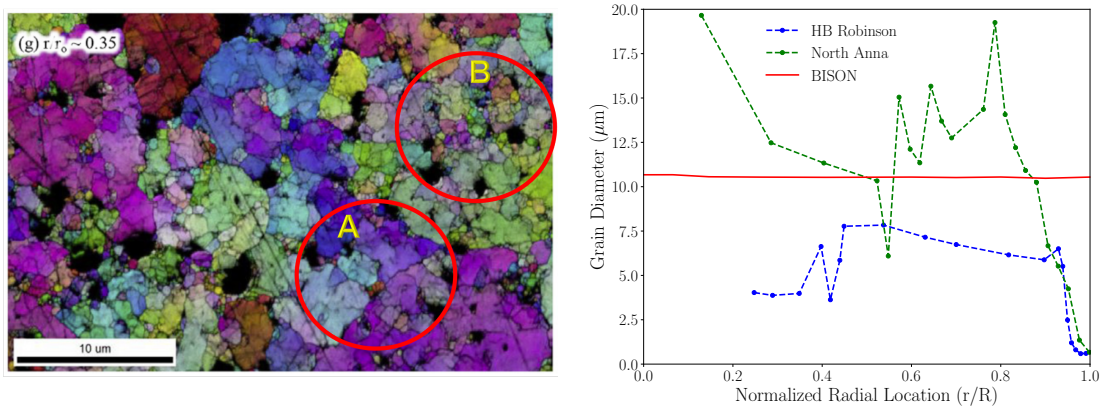

(a) (b)

Figure 17. (a) Microstructure observed in the dark zones of HB Robinson Fuel [3]. (b) Comparison of grain size variations across radial direction observed in experiments (reproduced from [1] using Plotdigitizer [2]).

Qualitatively, the simulated microstructures show similar characteristics as observed in Figure 17a. Here, Zone A and Zone B are representative of the partially restructured and fully restructured regions. It is observed that the restructuring initiates around the existing bubbles. Furthermore, different regions have reached different levels of restructuring within the same micrograph. This indicates that there is a bias depending on damage accumulation within the grains and bubble distribution. The current model appropriately captures both of these phenomenon as observed in Figure 5 and Figure 11. The average grain diameter achieved in the simulations vary from 1 μm to 3.5 μm. The maximum grain diameter observed corresponds to Case IV presented in Section 3.2 (Figure 11). This value is close to the grain diameter observed in the dark zone of the HBR fuel [1, 3].

4. CONCLUSION

In conclusion, this report summarizes the development of a novel phase-field based restructuring model to predict the restructuring observed closer to the fuel center known as the dark zone. In Section 3 we present how different parameters such as burnup rate, dislocation densities and temperature influence the subgrain formation rate and restructuring predicted at the mesoscale. It is demonstrated that qualitatively the model predicts similar characteristics as observed in experiments. The key findings are listed below:

- Subgrain formation begins around exising fission gas bubbles and then proceeds towards triple junctions, grain boundaries and grain interiors.
- A restructuing bias is observed within the microstructure due to variation in defect accumulation among different grains.
- Restructuring is influenced by a combination of initial dislocation densities, subgrain formation rate, and temperature.
- Rate of restructuring increases with increase in fuel temperature.

In the following years, the phase-field-based restructuring model will be extended to include the role of dislocation interaction and grain orientation to distinguish between different types of grain boundaries to better understand the restructuring that occurs both within the rim region and at the dark zone closer to the fuel center. Currently BISON does not have a restructuring model that can capture the dark zone behavior. Hence, a mesoscale-informed mechanistic model for restructuring needs to be implemented in BISON to improve its robustness. The fitting parameters calculated from this work (Table 5) will be provided to BISON. The BISON model for restructuring fraction and grain size evolution will be updated based on the mesoscale observations. Such updates are necessary to validate and improve BISON prediction for the fuel performance as a function of radial location. This would enable BISON to appropriately predict the effect of restructuring on the fission gas release.

[1] N. Capps, D. Schappel, C. McKinney, J. Harp, M. Cooper, D. Andersson, P. Simon, S. Novascone, Bison validation against pressurized water reactor high-burnup post-irradiation examination data, in: Proceedings of Top Fuel 2024, Grenoble, France, 2024.

[2] Plotdigitizer: Version 3.1.5 (2024).
URL https://plotdigitizer.com

[3] T. J. Gerczak, C. M. Parish, P. D. Edmondson, C. Balswin, K. A. Terrani, Restructuring in high burnup uo2 studied using modern electron microscopy, J. Nucl. Mat. 509 (2018) 246–259. doi:https://doi.org/10.1016/j.jnucmat.2018.05.077.

[4] V. V. Rondinella, T. Wiss, The high burn-up structure in nuclear fuel, Materials Today 13 (2010) 24–32.

[5] J. Noirot, I. Zacharie-Aubrun, T. Blay, Focused ion beamescanning electron microscope examination of high burn-up uo2 in the center of a pellet, Nuclear Engineering and Technology 50 (2018) 259–267. doi:https://doi.org/10.1016/j.net.2017.12.002.

[6] N. Capps, C. Jensen, F. Cappia, J. Harp, K. Terrani, N. Woolstenhulme, D. Wachs, A critical review of high burnup fuel fragmentation, relocation, and dispersal under loss-of-coolant accident conditions, Journal of Nuclear Materials 546 (2021) 152750. doi:https://doi.org/10.1016/j.jnucmat.2020.152750.

[7] Z. Xiao, Y. Wang, S. Hu, Y. Li, S.-Q. Shi, A quantitative phase-field model of gas bubble evolution in UO_2, Computational Materials Science 184 (2020) 109867.

[8] C. Smith, S. Biswas, B. D. Miller, B. Kombaiah, D. Frazer, D. D. Keiser, A. Aitkaliyeva, Investigation of high burnup structure in u-mo fuels, Journal of Nuclear Materials 563.

[9] L. K. Aagesen, Y. Gao, D. Schwen, K. Ahmed, Grand-potential-based phase-field model for multiple phases, grains, and chemical components, Physical Review E 98 (2018) 023309.

[10] S. Gentry, K. Thornton, Simulating recrystallization in titanium using the phase field method, in: IOP Conference Series: Materials Science and Engineering, Vol. 89, IOP Publishing, 2015, p. 012024.

[11] L. K. Aagesen, D. Schwen, M. R. Tonks, Y. F. Zhang, Phase-field modeling of fission gas bubble growth on grain boundaries and triple junctions in UO_2 nuclear fuel, Computational Materials Science 161 (2019) 35–45.
URL <GotoISI>://WOS:000462165100005

[12] C. Matthews, R. Perriot, M. W. D. Cooper, C. R. Stanek, D. A. Andersson, Cluster dynamics simulation of xenon diffusion during irradiation in UO_2, Journal of Nuclear Materials in press (2020) 152326.

[13] L. Yang, B. W. Wirth, An improved xenon equation of state for nanobubbles in uo_2, Journal of Nuclear Materials 572 (2022) 154089.

[14] S. Biswas, L. K. Aagesen, W. Jiang, C. O. Galvin, M. W. D. Cooper, Multiscale modeling for high burnup structure formation and associated pulverization, Tech. Rep. INL/RPT-23-74953, Idaho National Laboratory (2023).

[15] N. Moelans, B. Blanpain, P. Wollants, Quantitative analysis of grain boundary properties in a generalized phase field model for grain growth in anisotropic systems, Phys. Rev. B 78 (2008) 024113.

[16] J. Ainscough, B. Oldfield, J. Ware, Isothermal grain growth kinetics in sintered UO_2 pellets, Journal of Nuclear Materials 49 (2) (1973) 117–128.

[17] L. K. Aagesen, S. Biswas, W. Jiang, D. Andersson, M. W. D. Cooper, C. Matthews, Mesoscale simulations to inform microstructure- based pulverization criterion in high-burnup uo_2, Tech. Rep. INL/EXT-21-64275, Idaho National Laboratory (2021).

[18] C. Matthews, R. Perriot, M. W. D. Cooper, C. R. Stanek, D. A. Andersson, Cluster dynamics simulation of uranium self-diffusion during irradiation in UO_2, Journal of Nuclear Materials 527 (2019) 151787.

[19] H. Matzke, Radiation enhanced diffusion in UO2 and (U, Pu)O2, Radiation Effects 75 (1-4) (1983) 317–325. doi:10.1080/00337578308224715.
URL https://doi.org/10.1080/00337578308224715

[20] L. K. Aagesen, Parameterization of vacancy production rate in phase-field models of fission gas bubble evolution in nuclear fuel, Journal of Nuclear Materials 601 (2024) 155311. doi:https://doi.org/10.1016/j.jnucmat.2024.155311.

[21] D.R.Olander, Fundamental aspects of nuclear reactor fuel elements, Technical Information Center, Office of Public Affairs Energy Research and Development Administration, 1976.

[22] T. Takaki, Y. Tomita, Static recrystallization simulations starting from predicted deformation microstructure by coupling multi-phase-field method and finite element method based on crystal plasticity, International Journal of Mechanical Sciences 52 (2) (2010) 320–328.

[23] K. Nogita, K. Une, Irradiation-induced recrystallization in high burnup UO_2 fuel, Journal of Nuclear Materials 226 (3) (1995) 302–310. doi:10.1016/0022-3115(95)00123-9.

[24] M. Idiri, T. Le Bihan, S. Heathman, J. Rebizant, Behavior of actinide dioxides under pressure: UO_2 and ThO_2, Physical Review B 70 (1).
URL <GotoISI>://WOS:000222996300040

[25] J. B. Wachtman, M. L. Wheat, H. J. Anderson, J. L. Bates, Elastic constants of single crystal UO_2 at 25 degrees C, Journal of Nuclear Materials 16 (1) (1965) 39–41.
URL <GotoISI>://WOS:A19657630000005

[26] L. K. Aagesen, S. Biswas, K. A. Gamble, W. Jiang, P.-C. Simon, B. W. Spencer, Implementation and testing of physics-based pulverization model in bison, Tech. Rep. INL/RPT-22-67941, Idaho National Laboratory (2022).

[27] D. Knoll, D. Keyes, Jacobian-free newton-krylov methods: a survey of approaches and applications, J. Comput. Phys. 193 (2004) 357–397.
URL https://www.sciencedirect.com/science/article/pii/S0021999103004340

[28] B. S. Kirk, J. W. Peterson, R. H. Stogner, G. F. Carey, libMesh: a C++ library for parallel adaptive mesh refinement/coarsening simulations, Engineering with Computers 22 (2006) 237–254. doi:0.1007/s00366-006-0049-3.

[29] T. Barani, G. Pastore, D. Pizzocri, D. Andersson, C. Matthews, A. Alfonsi, K. Gamble, P. V. Uffelen, L. Luzzi, J. Hales, Multiscale modeling of fission gas behavior in u3si2 under lwr conditions, Journal of Nuclear Materials 522 (2019) 97 – 110. doi:10.1016/j.jnucmat.2019.04.037.